Influence of Topological Confinement on Nanoscale Film Morphologies of Tricyclic Block Copolymers

Brian J. Ree[1]*, Yusuke Satoh*[2]*, Takuya Isono*[1] *and Toshifumi Satoh*[1,*]

[1]Faculty of Engineering, Hokkaido University, Sapporo 060-8628, Japan

[2]Graduate School of Chemical Sciences and Engineering, Hokkaido University, Sapporo 060-8628, Japan

*Correspondence to: satoh@eng.hokudai.ac.jp (T.S.)

ABSTRACT: This study is the first quantitative synchrotron grazing incidence X-ray scattering investigation of nanoscale film morphologies of tricyclic block copolymers based on poly(*n*-decyl glycidyl ether) (PDGE) and poly(2-(2-(2-methoxyethoxy)ethoxy)ethyl glycidyl ether) (PTEGGE) blocks in equivalent volume fractions. Both PDGE and PTEGGE blocks of the tricyclic block copolymers are amorphous but copolymers exhibit phase-separated lamellar nanostructures due to block immiscibility. The lamellar structures vary in their structural parameters such as lamellar orientation, and structural integrity stability depending on the degree of topological confinement effect taking effect. Interestingly, sub-10 nm domain spacings are established by all nanostructures, which are remarkably shorter than that of the linear analogue. These exceptionally short domain spacings are evident that the tricyclic block copolymer approach is highly efficient for developing high performance nanolithographic materials for future advanced semiconductor applications.

Keywords: tricyclic block copolymers; various tricyclic topologies; synchrotron grazing incidence X-ray scattering; nanoscale film morphologies; structural parameters; exceptionally small domain spacing

INTRODUCTION

Since the discovery of cyclic poly(dimethylsiloxane) as the first synthetic cyclic polymer in 1946,[1-3] great research efforts were inspired to pursue the unique physical properties of cyclic polymers originating from the absence of chain ends.[4-12] Over the last two decades, the synthesis of cyclic polymers became sophisticated and efficient based on anionic, cationic, and radical polymerizations accompanied by ring-expansion reactions and end-group coupling reactions.[5-20] As a natural evolution from conventional cyclic polymer, trefoil-shaped (*i.e.*, tricyclic) polymers were theorized and proposed in many discussions along with bicyclic topology and other complex variations.[5-12] Through strategic reaction schemes and intricate molecular designs, multiple systems of tricyclic polymers were successfully synthesized: tricyclic polystyrenes,[21] tricyclic polytetrahydrofurans,[22] tricyclic poly(ε-caprolactone)s,[23] (cyclic polystyrene)-*block*-[cyclic poly(tert-butyl acrylate)]-*block*-[cyclic poly(methyl acrylate)],[24] [cyclic poly(decyl glycidyl ether)-*block*-[cyclic poly(dec-9-enyl glycidyl ether)-*block*-[cyclic poly(2-(2-(2-methoxyethoxy) ethoxy) ethyl glycidyl ether)]s,[25] and various topological tricyclic [poly(*n*-decyl glycidyl ether)]-*block*-[poly(2-(2-(2-methoxyethoxy)ethoxy)ethyl glycidyl ether)]s.[26]

While these reports have demonstrated in detail the synthesis of various homopolymers and block copolymers with tricyclic topology, the physical properties of these complex materials could seldom be explored. Given that conventional cyclic polymers exhibit unique properties, such as a higher glass transition temperature, a shorter radius of gyration, and a lower viscosity than the linear counterparts,[5-8,12-14,16-19] tricyclic polymers are hypothesized to reveal a similar trend. The validity and limits of this hypothesis, however, remain unconfirmed both experimentally and theoretically. Additionally, morphology is an intriguing fundamental aspect that differentiates tricyclic polymers from conventional cyclic polymers. Although both topologies share a unique trait that is the absence of chain end, tricyclic polymers are essentially consisting of three

macrocycles bound at a single junction point, resulting in a more restrictive chain conformation than a single macrocycle. Hence, one could easily expect the influence from tricyclic topology to reveal unique morphological behaviors. Moreover, comprehending the correlation between the tricyclic topology and morphology would aid in accurately describing the physical properties from a fundamental basis. Thus, there is a need for comprehensive morphological investigations of homopolymers and block copolymers possessing tricyclic topology.

This study reports the first quantitative investigation on the nanoscale film morphologies of tricyclic poly(*n*-decyl glycidyl ether-*block*-2-(2-(2-methoxyethoxy)ethoxy)ethyl glycidyl ether)s (PDGE-*b*-PTEGGE), namely *Tricycle*-A, *Tricycle*-B, and *Tricycle*-C (Figure 1; Table S1 in Supporting Information), *via* synchrotron grazing-incidence X-ray scattering (GIXS). All copolymers possess a narrow dispersity ($Đ$) of 1.03, and their PDGE and PTEGGE blocks are defined by near equivalent volume fractions and degree of polymerization of 50. The copolymers are differentiated by the arrangement of PDGE and PTEGGE blocks within the tricyclic topology as shown in Figure 1. The immiscibility of PDGE and PTEGGE blocks causes phase separation between the blocks and enables the self-assembly of lamellar structures inside nanoscale films. Interestingly, the lamellar structures of all tricyclic block copolymers reveal highly miniaturized domain spacings (*d*-spacing) when compared to the lamellar structure formed by the linear block copolymer counterpart (*l*-BCP) of same molecular weight. Moreover, the lamellar structures of tricyclic block copolymers exhibit higher levels of structural integrity and lamellar orientation than *l*-BCP. The degree of *d*-spacing reduction, structural integrity, lamellar orientation, and other structural parameters are varied among the copolymers, which demonstrate the dependency of morphological features on the block arrangement within tricyclic topologies. All the structural details are discussed in correlation with topological influences.

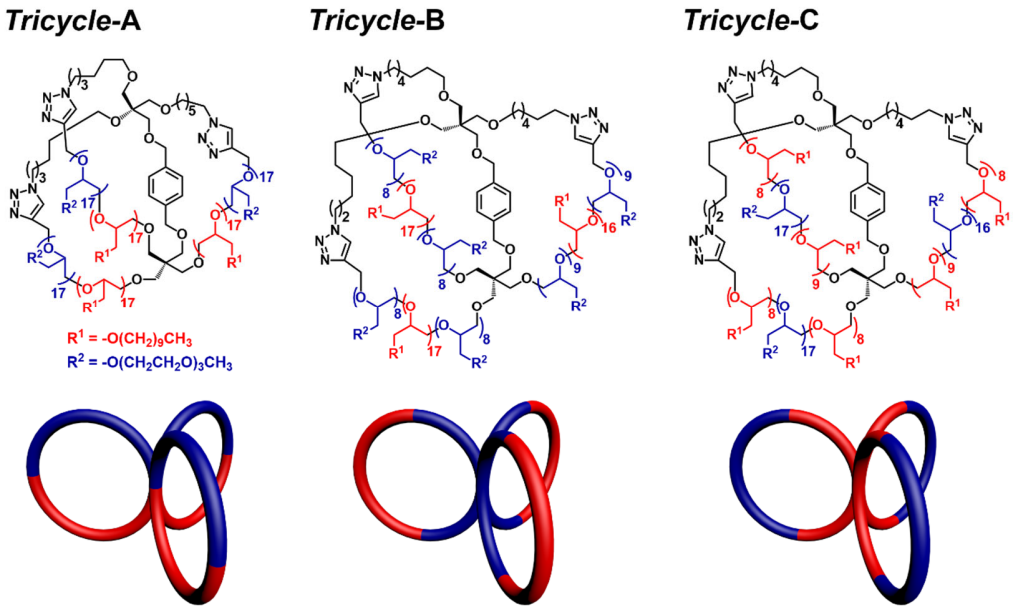

Figure 1. Chemical structures of tricyclic block copolymers in various topologies.

Table 1. Molecular characteristics of various topological tricyclic block copolymers and their homopolymers [a]

Polymer	$M_{n,NMR}$ [b] (g mol^{-1})	$Đ$ [c]	ρ_e [d] (nm^{-3})	ρ_m [e] (g cm^{-3})	PDGE block		PTEGGE block	
					DP_{PDGE} [f]	ϕ_{PDGE} [g]	DP_{PTEGGE} [h]	ϕ_{PTEGGE} [i]
Tricycle-A	22,900	1.03			51	0.504	51	0.496
Tricycle-B	22,700	1.03			50	0.504	50	0.496
Tricycle-C	22,200	1.03			50	0.504	50	0.496
c-PDGE	11,000	1.02	310	0.92				
l-PDGE	11,100	1.03	341	1.01				
l-PTEGGE	11,200	1.04	353	1.05				

[a]Data from reference no. 26 and 27. [b]Number-average molecular weight of polymer determined by ^{1}H NMR spectroscopic analysis. [c]Dispersity determined by size exclusion chromatography (SEC) analysis in tetrahydrofuran. [d]Electron density of homopolymers in films determined by X-ray reflectivity analysis. [e]Mass density of homopolymers in films obtained from the electron density determined by X-ray reflectivity analysis. [f]Number-average degree of polymerization of PDGE block determined by ^{1}H NMR spectroscopic analysis. [g]Volume fraction of PDGE block estimated from the $M_{n,NMR}$ and ρ_m data. [h]Number-average degree of polymerization of PTEGGE block determined by ^{1}H NMR spectroscopic analysis. [i]Volume fraction of PTEGGE block estimated from the $M_{n,NMR}$ and ρ_m data.

EXPERIMENTAL SECTION

Tricycle-A, *Tricycle*-B, and *Tricycle*-C were synthesized according to the synthetic schemes (Schemes S1–S3 in Supporting Information) reported previously.[26] The synthetic details are given with proton nuclear magnetic resonance (^{1}H NMR) and Fourier transform infrared (FT-IR) spectra and size exclusion chromatography (SEC) traces (Figures S1–S9) in Supporting Information and molecular characteristics of the copolymers are summarized in Table 1.

For each tricyclic block copolymer, differential scanning calorimetry (DSC) measurements were carried out with a ramping rate of 10 °C min^{-1} under nitrogen atmosphere using Hitachi instruments (model DSC7020, Hitachi Instrument, Tokyo, Japan).

For the individual copolymers, polymer solutions were prepared with a concentration of 0.5 wt% in tetrahydrofuran. The polymer solutions were filtered using disposable syringes equipped with polytetrafluoroethylene filter membranes of 0.2 μm pore size. Each polymer solution was deposited on silicon substrates by spin-coating and subsequent drying in vacuum at room temperature for 24 h. The thicknesses of the obtained films were measured using a spectroscopic ellipsometer (Model M-2000, Woollam, Lincoln, NE, USA); their thicknesses were in the range of 100–120 nm. All the film samples were stored in a drying chamber at room temperature before measurements.

Synchrotron grazing-incidence small-angle and wide-angle X-ray scattering (GISAXS and GIWAXS) measurements were conducted with an X-ray beam with wavelength (λ) of 0.12411 nm at the 3C beamline[27-30] of the Pohang Accelerator Laboratory (PAL), Pohang, Korea. The sample-to-detector distance (SDD) was set to 2951.3 mm and 214.7 mm for GISAXS and GIWAXS measurements, respectively. Each scattering image was collected for 10–30 s. The incidence angle α_i of the X-ray beam with respect to the film sample surface was set in the range of 0.1380–0.1850°,

which was between the critical angle of the polymer film and the silicon substrate ($\alpha_{c,f}$ and $\alpha_{c,s}$). Aluminium strips were used as a semi-transparent beam stop. A two-dimensional (2D) charge-coupled detector (CCD; model Rayonix 2D SX 165, Rayonix, Evanston, IL, USA) was used to measure all GIXS data. The scattering angles were corrected based on the positions of the X-ray beams reflected from the silicon substrate, and the peaks generated by precalibrated standards, which were polystyrene-*block*-poly(ethylene-*random*-butylene)-*block*-polystyrene and silver behenate standards (Tokyo Chemical Inc., Tokyo, Japan).

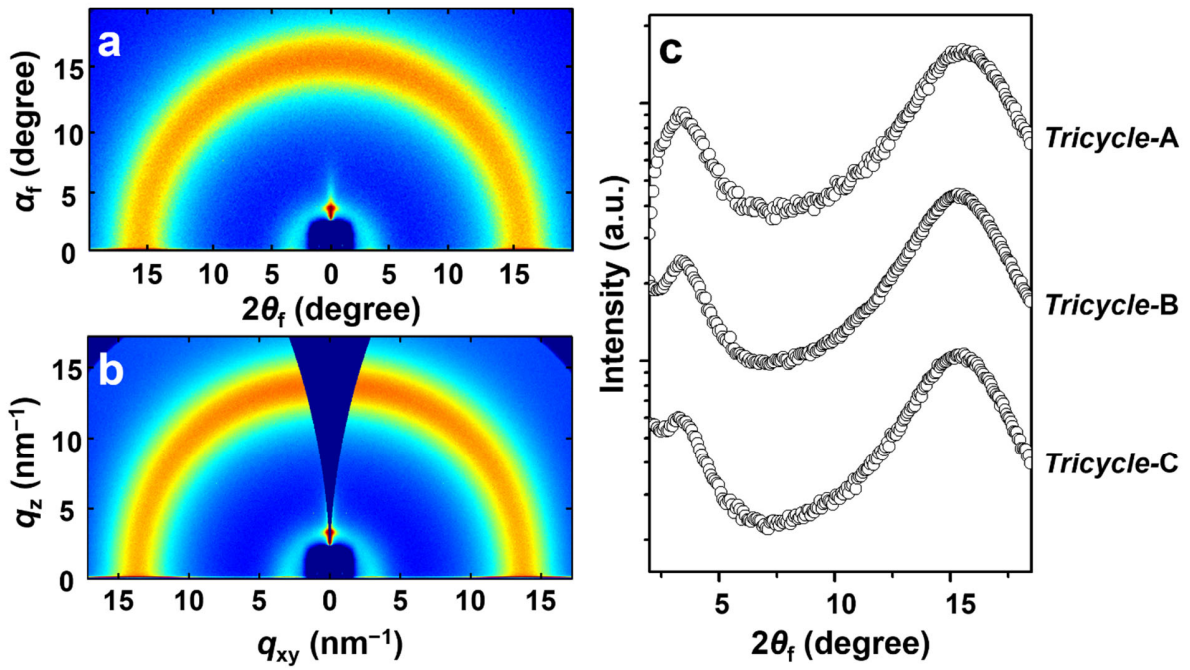

Figure 2. Representative GIWAXS data of the nanoscale films (100–120 nm thick) of tricyclic block copolymers measured with SDD = 214.7 mm at room temperature using a synchrotron X-ray beam (λ = 0.12411 nm): (a) 2D scattering image in angle space ($2\theta_f$ and α_f) of *Tricycle*-A (α_i = 0.1845°); (b) 2D scattering image in scattering vector space (q_{xy} and q_z) obtained from the scattering image in (a); (c) in-plane scattering profiles extracted along the equatorial line at α_f = 0.290° from the measured 2D scattering images for each block copolymer, including the image in (a).

RESULTS AND DISCUSSION

The DSC thermograms of copolymers show that their glass transitions and crystal melting points occur below −67.0 °C and 23.3 °C, respectively (Figure S10 and Table S1). Because all phase transitions occur below 23.3 °C, the 100–120 nm copolymer films were considered to be thermally annealed throughout the drying process and the storage period prior to GISAXS and GIWAXS measurements, which were also conducted at room temperature.

A representative 2D GIWAXS image of the *Tricycle*-A nanoscale films (Figures 2a and 2b) revealed two isotropic scattering peaks at approximately 3.4° (*d*-spacing = 2.1 nm) and 15.4° (*d*-spacing = 0.46 nm). These two isotropic peaks are commonly referred to as amorphous halos, which are also observed for *Tricycle*-B and *Tricycle*-C (GIWAXS images not shown). The in-plane scattering profiles extracted from the measured data are compared in Figure 2c, in which the peak near 3.0° can be assigned to the mean interdistance between the polymer chains, and the peak near 15° corresponds to the mean intramolecular and intermolecular interdistances between *n*-decyl and 2-(2-(2-methoxyethoxy)ethoxy)ethyl bristles. Overall, PDGE and PTEGGE blocks of all tricyclic block copolymers are confirmed by the GIWAXS measurements to be amorphous in the nanoscale films at room temperature.

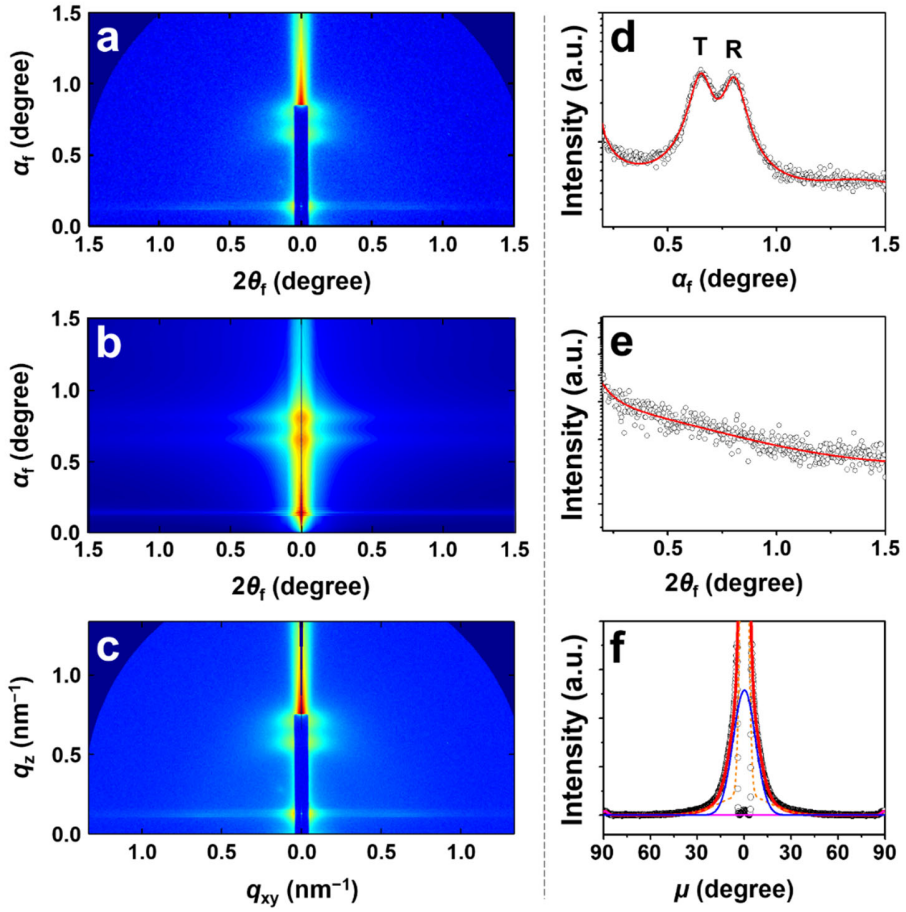

Figure 3. Representative GISAXS data of *Tricycle*-A films (100–120 nm thick) measured with α_i = 0.1461°; SDD = 2951.3 mm at room temperature using a synchrotron X-ray beam (λ = 0.12411 nm): (a) 2D scattering image in angle space. (b) 2D scattering image reconstructed with the structural parameters from data analysis. (c) 2D scattering image corrected and remapped to scattering vector space from (a). (d) 1D out-of-plane scattering profile obtained from the meridian line at $2\theta_f$ = 0.177° of (a). (e) 1D in-plane scattering profile obtained from equatorial line at α_f = 0.192° of (a). In (d) and (e), open circles are the measured scattering intensities and solid red lines represent the calculated intensities based on the GIXS formula of lamellar structure model; the scattering peaks generated by the reflected and transmitted X-ray beam are marked with "R" and "T", respectively. (f) Azimuthal scattering profile obtained along the azimuth at q = 0.712 nm^{-1} of (c) where the open circles represent measured intensities and the lines were obtained via deconvolution: the blue solid line represents the scattering peak of lamellae, the orange dotted line represents the intensities of the reflected X-ray beam, the magenta line represents the Yoneda peak, and the red solid line is the sum of all deconvoluted peaks.

Figure 3a presents a representative 2D GISAXS image of *Tricycle*-A films. The scattering image exhibits a pair of scattering peaks along the meridian line. Considering the GISAXS optics, the pair of scattering peaks are the result of peak splitting phenomenon, which occurs specifically

for in-plane oriented (*i.e.* horizontal) nanostructures. Hence, two peaks at $\alpha_f = 0.66°$ and $\alpha_f = 0.80°$ originate from the reflected and transmitted X-ray beams, respectively. Overall, this fully anisotropic image is a typical example of scattering pattern generated by a horizontally-oriented lamellar structure. Based on the GIXS formula of lamellar structure model (see Figure S11 and the details of the formula in Supporting Information), the one-dimensional (1D) scattering profiles extracted along the meridian line at $2\theta_f = 0.177°$ and along the equatorial line at $\alpha_f = 0.192°$ from the 2D image, are successfully analyzed (Figures 3d and 3e). The analysis confirms the presence of lamellar nanostructure in the film, and the additional analysis on the azimuthal scattering profile extracted at $q = 0.712$ nm^{-1} (Figure 3f) from the q-space image in Figure 3c confirms that the lamellar structure in the film has horizontal orientation. The obtained structural details are summarized in Table 2. Figure 3b presents a 2D scattering image reconstructed from the obtained structural parameters using the GIXS formula. This reconstructed image is well matched with the measured 2D scattering pattern and consequently assures confidence in the data analysis.

The quantitative analysis of GISAXS image in Figure 3 found that the nanostructure in the film consists of horizontal lamellae with a long period D_L of 9.80 nm. Each lamella is composed of three sublayers l_1, l_2, and l_3 of 2.30 nm, 2.70 nm, and 2.10 nm. Taking into account the volume fraction of the PDGE block which is slightly larger than that of the PTEGGE block for *Tricycle*-A, the l_1 and l_3 sublayers can be assigned to the PDGE and PTEGGE blocks, respectively. l_2 sublayer, as a result, is the interface between PDGE and PTEGGE sublayers. Here, it is noteworthy that the $D_{L,Tricycle\text{-}A}$ (9.80 nm) is a short d-spacing considering that the total molecular weight of *Tricycle*-A is 22,900 g mol^{-1}. The linear diblock copolymer of same chemical composition and molecular weight (*linear*-PDGE-*b*-PTEGGE) forms a mixture of horizontal and vertical lamellae with D_L of 24.0–25.5 nm.[31] Compared to the linear counterpart, the d-spacing reduction achieved by *Tricycle*-A is 59.2–61.6 %. This d-spacing reduction is greater than those reported experimentally (5–16 %) and theoretically (30–37 %) in the literature for conventional cyclic

block copolymers (*i.e.* a single macrocycle).[32-39] Interestingly, we have previously reported the nanoscale film morphologies of PDGE-*b*-PTEGGE bicyclic block copolymers in which 51.3–72.8 % *d*-spacing reduction was achieved against *linear*-PDGE-*b*-PTEGGE.[31] Considering the equivalent molecular weight among the bicyclic variations and *Tricycle*-A, the higher number of macrocycles in *Tricycle*-A yields a shorter length per each macrocycle compared to the bicyclic variations. This topological influence yields a direct consequence that is the *d*-spacing reduction. Moreover, the horizontal lamellae of *Tricycle-A* is characterized by the second order orientation factor O_s of 0.977, which indicates that the horizontal orientation is reasonably controlled by the tricyclic topology. However, the lattice distortion factor *g* (*g*-factor) is somewhat large, with a value of 0.15. These results collectively inform that the *Tricycle*-A lamellae show preference for horizontal orientation and achieve reasonable level of structural integrity. From all structural parameters determined above, a schematic nanostructure could be visualized for the nanoscale film morphology of *Tricycle*-A, as shown in Figure 4a.

Table 2. Morphological parameters of nanoscale films (100–120 nm thick) of various topological tricyclic block copolymers

Nanoscale film morphology	Tricyclic block copolymers				
	Tricycle-A 	*Tricycle*-B 		*Tricycle*-C 	
Lamellar Orientation	Horizontal	Horizontal	Vertical	Horizontal	Vertical
D_L[a] (nm)	9.80 (1.92)[j]	6.05 (1.02)	6.00 (1.14)	6.10 (0.60)	6.10 (0.71)
l_1[b] (nm)	2.30 (1.10)	1.50 (0.40)	1.50 (0.40)	1.80 (0.30)	1.60 (0.40)
l_2[c] (nm)	2.70 (0.80)	1.50 (0.60)	1.50 (0.70)	1.20 (0.30)	1.40 (0.30)
l_3[d] (nm)	2.10 (1.36)	1.55 (0.72)	1.50 (0.81)	1.90 (0.42)	1.70 (0.50)
g[e]	0.15	0.14	0.21	0.30	0.24
$\overline{\varphi}$[f] (deg.)	0	0	89.2	0	90
σ_ϕ[g] (deg.)	7.20	1.10	0.50	18.62	27.73
O_s[h]	0.977	0.992	−0.497	0.790	−0.210
ϕ[i] (vol%)	100	99.9	0.1	41.1	58.9

[a]Long period of lamellar structure. [b]Thickness of the l_1 layer. [c]Thickness of the l_2 layer, i.e., interfacial layer. [d]Thickness of the l_3 layer. [e]Lattice distortion factor of nanostructure (i.e., lamellar structure) along the *z*-

axis which is parallel to the out-of-plane of the film. [f]Mean value of the polar angle φ (i.e., orientation angle) between the orientation vector $\boldsymbol{n}$ (which is set along a direction normal to the in-plane of lamellar structure) and the out-of-plane direction of the film. [g]Standard deviation for the polar angle φ. [h]Second order orientation factor of nanostructure (i.e., lamellar structure). [i]Volume fraction in percent. [j]Standard deviation.

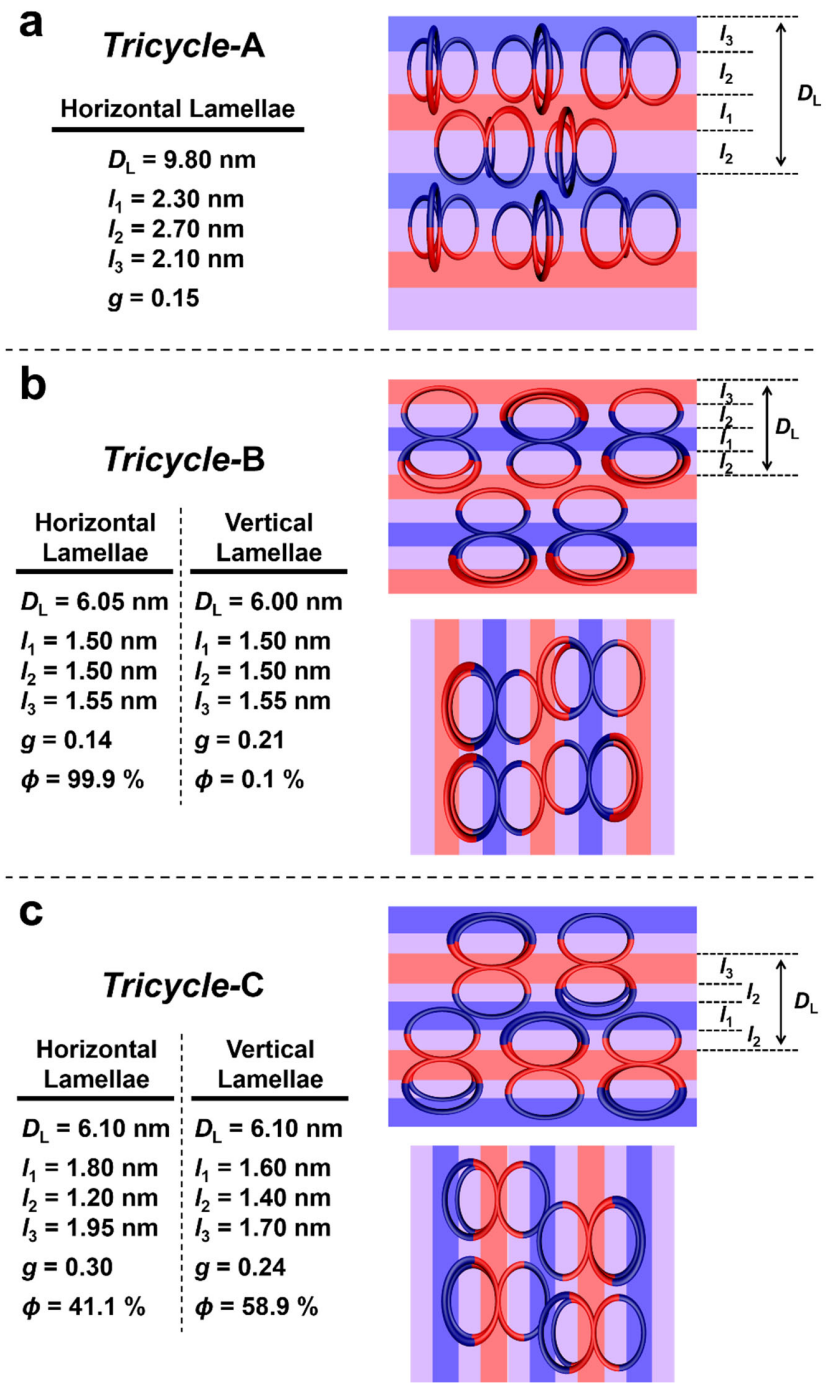

Figure 4. Schematic representations of nanostructures (cross-sectional view) inside topological block copolymer films. (**a**) Horizontal lamellae inside *Tricycle*-A film where the blue sublayer is assigned to

PTEGGE blocks and the red sublayer is assigned to PDGE block. (**b**) Horizontal and vertical lamellae inside *Tricycle*-B film where the blue sublayer is assigned to PTEGGE blocks and the red sublayer is assigned to PDGE block. (**c**) Horizontal and vertical lamellae inside *Tricycle*-C film where the blue sublayer is assigned to PTEGGE blocks and the red sublayer is assigned to PDGE block.

The nanoscale films of *Tricycle*-B also exhibit a clearly distinctive GISAXS pattern (Figure 5a) that is typical of horizontal lamellae. The scattering image apparently resembles that of the *Tricycle*-A film, but the position of the pair of peaks (α_f = 1.09°, 1.25°) occurring along the meridian line is different. With this information, the scattering image was analyzed in a manner similar to that employed for the *Tricycle*-A film. The 1D scattering profiles extracted from the 2D scattering image are satisfactorily analyzed by the GIXS formula based on lamellar structure model (Figures 5d and 5e). The azimuthal scattering profile extracted from the 2D image in the q-space (Figure 5b) at q = 1.10 nm^{-1} could be analyzed successfully (Figure 5f). The obtained structural details are summarized in Table 2.

The GISAXS analysis identifies a mixture of horizontal and vertical lamellae in *Tricycle*-B films. Based on the analysis of azimuthal scattering profile, horizontal lamellae are the dominant structure with 99.9 vol% and the remaining 0.1 vol% is attributed to the vertical lamellae. The horizontal lamellae is characterized by the following parameters: D_L = 6.05 nm, l_1 = 1.50 nm, l_2 = 1.50 nm, l_3 = 1.55 nm, O_s = 0.992, and g = 0.14. The vertical lamellae exhibits near identical structural parameters with the exception of a greater g-factor value of 0.21. Taking into account the volume fractions of the blocks, the l_1 and l_3 sublayers can be assigned by the PTEGGE and PDGE block chain phases, respectively, and the l_2 sublayer as the interfacial layer. A 2D scattering image has been reconstructed with the determined structural parameters using the GIXS formula (Figure 5b). The reconstructed image is in good agreement with the measured data in Figure 5a. With these structural analysis results, a schematic nanostructure could be visualized for the morphology of the *Tricycle*-B film (Figure 5b). Overall, the *Tricycle*-B film reveals a lamellar morphology similar to that observed in the *Tricycle*-A film, but with several key differences. In particular, $D_{L,Tricycle\text{-}B}$ is shorter than $D_{L,Tricycle\text{-}A}$ by 38.3–38.8 % and the horizontal lamellae of

Tricycle-B reveals a better orientation than that of *Tricycle*-A ($O_{s,Tricycle\text{-}A}$ = 0.977; $O_{s,Tricycle\text{-}B}$ = 0.992). Furthermore, *Tricycle*-B achieves a *d*-spacing reduction of 74.8–76.3 % when compared against the linear counterpart. This value is quite remarkable, as it surpasses the previously reported maximum *d*-spacing reduction of 72.8 % achieved by bicyclic variations.[31] Given the very similar *g*-factors of the horizontal lamellae of *Tricycle*-A and -B ($g_{Tricycle\text{-}A}$ = 0.15; $g_{Tricycle\text{-}B}$ = 0.14), the particular arrangement of PDGE and PTEGGE blocks in *Tricycle*-B is more effective in reducing *d*-spacing while improving lamellar orientation and maintaining structural ordering of lamellar stacks. The only shortcoming of *Tricycle*-B is that it does not achieve a perfect orientation control, but volume fraction of the minor vertical lamellae is a negligible value of 0.1 vol%.

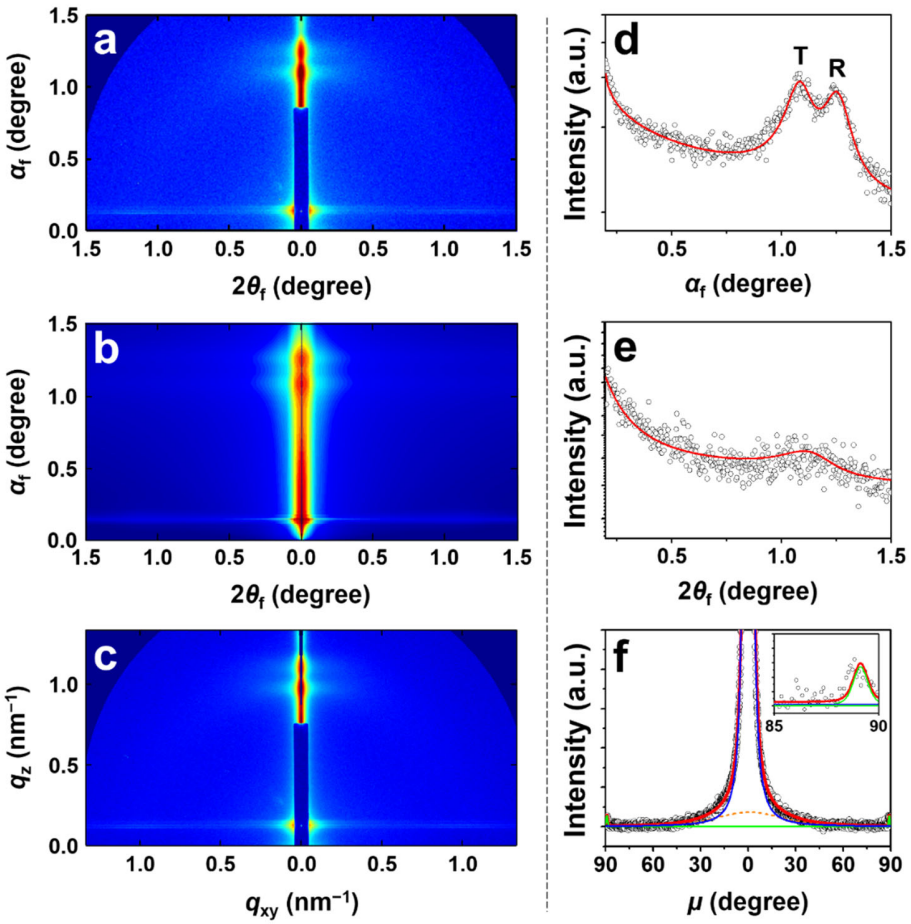

Figure 5. Representative GISAXS data of *Tricycle*-B films (100–120 nm thick) measured with α_i = 0.1476°; SDD = 2951.3 mm at room temperature using a synchrotron X-ray beam (λ = 0.12411 nm): (a)

2D scattering image in angle space. (b) 2D scattering image reconstructed with the structural parameters from data analysis. (c) 2D scattering image corrected and remapped to scattering vector space from (a). (d) 1D out-of-plane scattering profile obtained from the meridian line at $2\theta_f = 0.117°$ from (a). (e) 1D in-plane scattering profile obtained from equatorial line at $\alpha_f = 0.191°$ from (a). In (d) and (e), open circles are the measured scattering intensities and solid red lines represent the calculated intensities based on the GIXS formula of lamellar structure model; the scattering peaks generated by the reflected and transmitted X-ray beam are marked with "R" and "T", respectively. (f) Azimuthal scattering profile obtained along the azimuth at $q = 1.100$ nm^{-1} of (c) where the open circles represent measured intensities and the lines were obtained via deconvolution: the blue and green solid lines represent the scattering peaks of horizontal and vertical lamellae, respectively, the orange dotted line represents the intensities of the reflected X-ray beam, the magenta line represents the Yoneda peak, and the red solid line is the sum of all deconvoluted peaks.

Figure 6a displays a representative scattering image of the *Tricycle*-C films, which is different from those of the *Tricycle*-A and -B films. The 2D scattering image reveals one scattering peak appearing around 1.10° (= $2\theta_f$) along the equatorial line, and another appearing around 1.02° (= α_f) along the meridian line, with the former exhibiting a relatively stronger intensity than the latter. The two peaks are indicative of vertical and horizontal lamellae existing inside the film. In addition, the fact that the peaks are conjoined into a scattering ring indicates that there are relatively large levels of distribution in the vertical and horizontal orientation of lamellar structures (*i.e.* low degrees of orientation control). To parameterize the lamellar structure of *Tricycle*-C, the scattering pattern was analyzed in a similar fashion as the other tricyclic counterparts. The 1D scattering profiles extracted along the meridian line at $2\theta_f = 0.071°$ and along the equatorial line at $\alpha_f = 0.200°$ from Figure 6a have been fitted by the GIXS formula derived with lamellar model (Figures 6d and 6e). Moreover, an azimuthal scattering profile extracted at $q = 0.977$ nm^{-1} from the q-space image (Figure 6c) has been analyzed in a quantitative manner (Figure 6f). The determined structural details are listed in Table 2. With these structural analysis results, a schematic nanostructure could be visualized for the morphology of the *Tricycle*-C film (Figure 4c).

The analysis of azimuthal scattering profile found the vertical and horizontal lamellae are present inside the film with volume fractions of 58.9 % and 41.1 %, respectively. The vertical

lamellae are characterized with D_L = 6.10 nm, l_1 = 1.80 nm, l_2 = 1.20 nm, and l_3 = 1.90 nm. D_L and sublayer thicknesses are similar to that of *Tricycle*-B, which is not a surprising result considering that the arrangement of PDGE and PTEGGE blocks of *Tricycle*-C is the opposite of *Tricycle*-B. However, *g*-factors of both vertical and horizontal lamellae of *Tricycle*-C ($g_{Tricycle\text{-}C}$ = 0.30, 0.24) are larger than that of *Tricycle*-B ($g_{Tricycle\text{-}B}$ = 0.14, 0.20), indicating that the structural ordering between the two tricyclic counterparts differ rather substantially. Between the two orientations, the vertical lamellae exhibit a relatively better structural ordering. However, the vertical lamellae also reveal a larger σ_φ (the standard deviation of the polar angle φ between the orientation vector $\boldsymbol{n}$ set along a direction normal to the in-plane of lamellar structure and the out-of-plane direction of the film; see Figure S12), compared to that of the horizontal lamellae. In other words, vertical lamellae possesses a lower orientation control than horizontal lamellae.

Considering the similar degrees of polymerization and volume fractions for PDGE and PTEGGE blocks, the apparent differences in the morphological features, especially *d*-spacing, g-factor, and structural orientation, among *Tricycle*-A, *Tricycle*-B, and *Tricycle*-C are noteworthy. First of all, *Tricycle*-A forms the largest lamellae out of the three tricyclic variations in this study. This is due to the fact that PDGE and PTEGGE blocks are arranged in an equatorial division for *Tricycle*-A, whereas *Tricycle*-B and *Tricycle*-C have their blocks arranged in a meridian division as shown in Figure 1. This results in an interesting phenomenon where the molecular joint conjoining the three macrocycles for *Tricycle*-A is positioned in the interface between PDGE and PTEGGE sublayers (*i.e.* l_2 sublayer) whereas the molecular joints of *Tricycle*-B and *Tricycle*-C reside within either PDGE or PTEGGE sublayer. This particular point of contrast between *Tricycle*-A versus *Tricycle*-B and *Tricycle*-C—topological confinement effect—is the source of morphological differences in the lamellar structures of tricyclic block copolymers. *Tricycle*-A exhibits topological confinement through enlarged interface where the thickness of l_2 sublayer is

greater than both of its PDGE and PTEGGE sublayers (see Table 2), as opposed to *Tricycle*-B and *Tricycle*-C revealing l_2 sublayers with similar thickness as their PDGE and PTEGGE sublayers. The thicker interface formed by *Tricycle*-A is caused by portions of PDGE and PTEGGE blocks near the molecular joint experiencing restricted chain conformation and mobility. Moreover, as a consequence of conformational restriction at the molecular joint, each macrocycle of *Tricycle*-A are slightly elongated in the meridian direction with respect to the chemical structure of the block copolymer, thereby resulting in the longest *d*-spacing among all copolymers.

On the other hand, *Tricycle*-B and *Tricycle*-C experience topological confinement in a different manner where only either PDGE or PTEGGE block conjoined by the molecular joint is affected. Given their particularly complex block arrangement, the similar meridian direction biased chain conformation promotes shorter *d*-spacings than *Tricycle*-A lamellae. Interestingly, *Tricycle*-B and *Tricycle*-C differ in their structural ordering as indicated by their *g*-factors. This indicates that PDGE and PTEGGE blocks experience different degrees of restricted chain conformation and mobility from topological confinement, with PDGE block receiving higher restriction evidenced by: $g_{Tricycle\text{-B}} < g_{Tricycle\text{-C}}$. Furthermore, another negative implication from the aforementioned restriction occurs in the lamellar orientation, in which *Tricycle*-C fails to exhibit any orientation control. The seemingly opposite outcomes of the topological confinement on PDGE and PTEGGE blocks may be correlated to their chemical structures. Although both blocks share the same polyether backbone, *n*-decyl bristles of PDGE blocks are saturated hydrocarbons with a sufficient length for exhibiting a relatively greater stiffness (*i.e.* longer persistence length) than the 2-(2-(2-methoxyethoxy)ethoxy)ethyl bristles in PTEGGE blocks. Hence, the relatively stiffer PDGE block in *Tricycle*-C suffers a loss in structural ordering due to topological frustration, whereas PTEGGE block in *Tricycle*-B is able to relieve the frustration through its flexibility and maintain structural ordering of its lamellae. The discussion regarding topological confinement is, however, built only

on GISAXS characterization results, and additional theoretical and experimental investigations are necessary in order to determine the extent of thermodynamic aspects of complex tricyclic topology. Overall, the particular tricyclic topology of *Tricycle*-B is noteworthy as it demonstrated the formation of well-defined horizontal lamellae with the shortest *d*-spacing among all copolymers in this study. With the consideration of the expected full pitch dimension (*i.e. d*-spacing) of microprocessors ranges 7–8 nm by 2030 announced by International Roadmap for Devices and Systems (IRDS),[40] *Tricycle*-B is indeed a contender as the molecular platform for developing highly ordered nanolithographic materials.

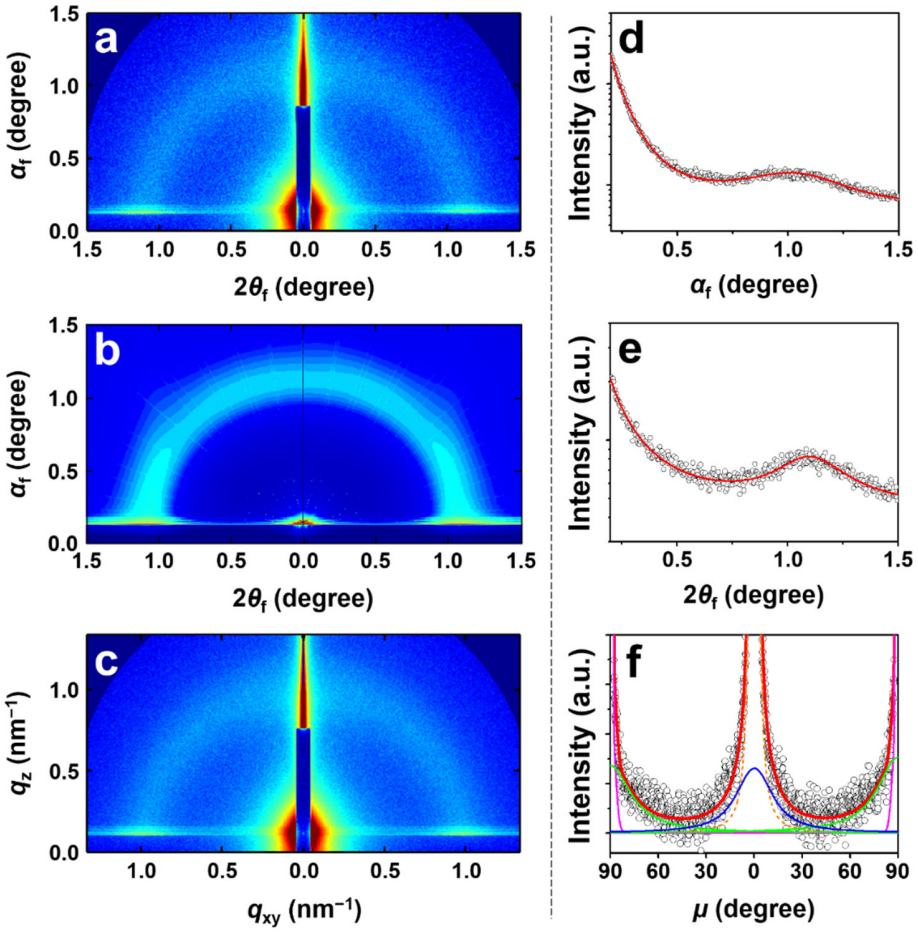

Figure 6. Representative GISAXS data of *Tricycle*-C films (100–120 nm thick) measured with $\alpha_i = 0.1384°$; SDD = 2951.3 mm at room temperature using a synchrotron X-ray beam ($\lambda = 0.12411$ nm): (a) 2D scattering

image in angle space; (b) 2D scattering image reconstructed with the structural parameters from data analysis. (c) 2D scattering image corrected and remapped to scattering vector space from (a). (d) 1D out-of-plane scattering profile obtained from the meridian line at $2\theta_f$ = 0.071° from (a). (e) 1D in-plane scattering profile obtained from equatorial line at α_f = 0.200° from (a). In (d) and (e), open circles are the measured scattering intensities and solid red lines represent the calculated intensities based on the GIXS formula of lamellar structure model. (f) Azimuthal scattering profile obtained along the azimuth at q = 0.977 nm^{-1} of (c) where the open circles represent measured intensities and the lines were obtained via deconvolution: the blue and green solid lines represent the scattering peaks of horizontal and vertical lamellae, respectively, the orange dotted line represents the intensities of the reflected X-ray beam, the magenta line represents the Yoneda peak, and the red solid line is the sum of all deconvoluted peaks.

CONCLUSIONS

Three different tricyclic topologies of PDGE and PTEGGE blocks in equivalent volume fractions were investigated in detail by synchrotron GIXS analysis. The quantitative GIXS analysis provides the morphological details of the complex tricyclic block copolymers in nanoscale films.

Both PDGE and PTEGGE blocks of all three copolymers are amorphous at room temperature. However, their phase-separation drives the self-assembly of lamellar nanostructures through the film fabrication processes. The structural integrity, orientation, and dimensional parameters of the lamellar nanostructure are varied between the three molecular topologies as a result of topological confinement effect. In particular, topological confinement takes greatest effect in *Tricycle*-B and *Tricycle*-C where the relatively stiffer PDGE block of *Tricycle*-C produces loss of structural integrity and lamellar orientation whereas relatively more flexible PTEGGE block of *Tricycle*-B exhibits the opposite. In short, the structural integrity and orientation orders are in the increasing trend: *Tricycle*-C << *Tricycle*-A < *Tricycle*-B. The *d*-spacing follows the decreasing trend: *Tricycle*-A >> *Tricycle*-C $\geq$ *Tricycle*-B. Thusly, *Tricycle*-B demonstrates the most well-defined lamellar structure with the highest structural stability and orientation, as well as the shortest *d*-spacing.

All nanostructures of this study reveal exceptionally smaller domain spacings than that of the linear counterpart of identical chemical composition and molecular weight. The *d*-spacing

reductions achieved by tricyclic block copolymers range 59.2–76.3 %, which are remarkable results that surpasses the previously reported *d*-spacing reductions from conventional cyclic and bicyclic block copolymer systems. Moreover, the shortest *d*-spacing demonstrated in this study, 6.00 nm, is shorter than the microprocessor pitch dimension predicted by International Roadmap for Devices and Systems (IRDS) for this decade.[40] Therefore, this study offers tricyclic block copolymers, *Tricycle*-B in particular, as strong contenders for the development of high performance nanolithographic materials.

ASSOCIATED CONTENT

Supporting Information

The Supporting Information is available free of charge on the ACS Publication website at DOI:10.1021/acs.macromol.xxxxx

Synthesis, synthetic schemes, ^{1}H NMR spectra, SEC traces, FT-IR spectra, DSC thermograms, thermal properties, and grazing incidence X-ray scattering data analysis.

AUTHOR INFORMATION

Corresponding Author

*E-mail: satoh@eng.hokudai.ac.jp. Phone:+81-11-706-6602. Fax: +81-11-706-6602 (T.S.)

ORCID

Brian J. Ree: 0000-0002-3959-9896

Takuya Isono: 0000-0003-3746-2084

Toshifumi Satoh: 0000-0001-5449-9642

Author Contributions

T.S. supervised the project. B.J.R., Y.S., and T.I. designed the experiments, solved the technical issues, and checked the experimental results. All authors contributed to developing the overall scope, interpreting the results and preparing the manuscript.

Notes

The authors declare no competing interests.

ACKNOWLEDGMENTS

This study was supported by JSPS Grant-in-Aid for Scientific Research (A and B) (19H00905 and 19H02769 for T.S.), MEXT Grant-in-Aid for Scientific Research on Innovative Areas “Hybrid Catalysis” (20H04789 for T.S.), JSPS Grant-in-Aid for Challenging Exploratory Research (19K22209 for T.S.), JST CREST (JPMJCR19T4 for T.S.), the Photoexcitonix Project (Hokkaido University, T. S.), Creative Research Institute (CRIS, Hokkaido University, T. S.), and the Frontier Chemistry Center (Hokkaido University, T. S., T. I., and B. J. R.). B. J. R. was funded by the JSPS Fellowship for Young Scientists. The authors thank the Pohang Accelerator Laboratory for providing opportunities to conduct synchrotron X-ray scattering measurements.

REFERENCES

(1) Patnode, W.; Wilcock, D. F. Methylpolysiloxanes. *J. Am. Chem. Soc.***1946**, *68*, 358−363.

(2) Hunter, M. J.; Hyde, J. F. Warrick, E. L.; Fletcher, H. J. Organo-silicon Polymers. The Cyclic Dimethyl Siloxanes. *J. Am. Chem. Soc.* **1946**, *68*, 667−672.

(3) Scott, D. W. Equilibria between Linear and Cyclic Polymers in Methylpolysiloxanes. *J. Am. Chem. Soc.* **1946**, *68*, 2294−2298.

(4) Zimm, B. H; Stockmayer, W. H. The Dimensions of Chain Molecules Containing Branches and Rings. *J. Chem. Phys*. **1949**, *17*, 1301−1314.

(5) Semlyen, J. A. Cyclic Polymers, 2nd ed., Kluwer Academic Publishers: Dordrecht, Netherlands, 2002.

(6) Laurent, B. A.; Grayson, S. M. Synthetic Approaches for the Preparation of Cyclic Polymers. *Chem. Soc. Rev.* **2009**, *38*, 2202–2213.

(7) Kricheldorf, H. R. Cyclic Polymers: Synthetic Strategies and Physical Properties. *J. Polym. Sci. Part A: Polym. Chem.* **2010**, *48*, 251− 284.

(8) Yamamoto, T.; Tezuka, Y. Topological Polymer Chemistry: A Cyclic Approach Toward Novel Polymer Properties and Functions. *Polym. Chem.* **2011**, *2*, 1930−1941.

(9) Lonsdale, D. E.; Monteiro, M. J. Synthesis and Self-assembly of Amphiphilic Macrocyclic Block Copolymer Topologies. *J. Polym. Sci. Part A: Polym. Chem.* **2011**, *49*, 4603–4612.

(10) Jia, Z.; Monteiro, M. J. Cyclic Polymers: Methods and Strategies. *J. Polym. Sci. Part A: Polym. Chem*. **2012**, *50*, 2085−2097.

(11) Jia, Z.; Monteiro, M. J. Synthesis of Cyclic Polymers via Ring Closure. *Adv. Polym. Sci.* **2013**, *262*, 295−328.

(12) Tezuka, Y. *Topological Polymer Chemistry: Progress of Cyclic Polymers in Syntheses, Properties and Functions*. World Scientific: Hackensack, NJ, USA, 2013.

(13) Isono, T.; Satoh, Y.; Miyachi, K.; Chen, Y.; Sato, S.-i.; Tajima, K.; Satoh, T.; Kakuchi, T. Synthesis of Linear, Cyclic, Figure-Eight-Shaped, and Tadpole Shaped Amphiphilic Block Copolyethers *via t*-Bu-P_4-Catalyzed Ring Opening Polymerization of Hydrophilic and Hydrophobic Glycidyl Ethers. *Macromolecules* **2014**, *47*, 2853−2863.

(14) Wang, H.; Zhang, L.; Liu, B.; Han, B.; Duan, Z.; Qi, C.; Park, D.; Kim, I. Synthesis of High Molecular Weight Cyclic Poly(ε-caprolactone)s of Variable Ring Size Based on A Light-Induced Ring-Closure Approach. *Macromol. Rapid Commun*. **2015**, *36*, 1646−1650.

(15) Zhao, Z.; Zhu, Q.; Wang, Z.; Lu, J.; Jin, Z.; Liu, H. A Dicyclic Scaffold for Programmed Monocyclic and Polycyclic Polymer Architectures. *Macromolecules* **2017**, *50*, 8907−8915.

(16) Xiang, L.; Ryu, W.; Kim, H.; Ree, M. Precise Synthesis, Properties, and Structures of Cyclic Poly(ε-caprolactone)s. *Polymers* **2018**, *10*, 577.

(17) Isono, T.; Sasamori, T.; Honda, K.; Mato, Y.; Yamamoto, T.; Tajima, K.; Satoh, T. Multicyclic Polymer Synthesis through Controlled/Living Cyclopolymerization of *α,ω*-Dinorbornenyl-Functionalized Macromonomers. *Macromolecules* **2018**, *51*, 3855–3864.

(18) Yamamoto, T.; Hosokawa, M.; Nakamura, M.; Sato, S.-i.; Isono, T.; Tajima, K.; S atoh, T.; Sato, M.; Tezuka, Y.; Saeki, A.; Kikkawa, Y. Synthesis, Isolation, and Properties of All Head-to-tail Cyclic Poly(3-hexylthiophene): Fully Delocalized Exciton over the Defect-Free Ring Polymer. *Macromolecules* **2018**, *51*, 9284–9293.

(19) Mato, Y.; Honda, K.; Tajima, K.; Yamamoto, T.; Isono, T.; Satoh, T. A Versatile Synthetic Strategy for Macromolecular Cages: Intramolecular Consecutive Cyclization of Star-shaped Polymers. *Chem. Sci.* **2019**, *10*, 440–446.

(20) Zhao, J.; Zhou, Y.; Li, Y.; Pan, X.; Zhang, W.; Zhou, N.; Zhang, K.; Zhang, Z.; Zhu, X. Modular Construction of Macrocycle-based Topological Polymers *via* High-efficient Thiol Chemistry. *Polym. Chem.* **2015**, *6*, 2879−2891.

(21) Lonsdale, D. E.; Monteiro, M. J. Various Polystyrene Topologies Built from Tailored Cyclic Polystyrene *via* CuAAC reactions. *Chem. Commun.* **2010**, *46*, 7945–7947.

(22) Tomikawa, Y.; Fukata, H.; Ko, Y. S.; Yamamoto, T.; Tezuka, Y. Construction of Double-Eight and Double-Trefoil Polymer Topologies with Core-clickable *Kyklo*-telechelic Precursors. *Macromolecules* **2014**, *47*, 8214-8223.

(23) Mato, Y.; Honda, K.; Ree, B. J.; Tajima, K.; Yamamoto, T.; Deguchi, T.; Isono, T.; Satoh, T. Programmed Folding into *Spiro*-multicyclic Polymer Topologies from Linear and Star-shaped Chains. *Chem. Comm.* **2020**, *3*, 97.

(24) Jia, Z. F.; Lonsdale, D. E.; Kulis, J.; Monteiro, M. J. Construction of a 3-miktoarm Star from Cyclic Polymers. *ACS Macro Lett.* **2012**, 1, 780–783.

(25) Shingu, T.; Yamamoto, T.; Tajima, K.; Isono, T.; Satoh, T. Synthesis of μ-ABC Tricyclic Miktoarm Star Polymer *via* Intramolecular Click Cyclization. *Polymers* **2018**, *10*, 877.

(26) Satoh, Y.; Matsuno, H.; Yamamoto, T.; Tajima, K.; Isono, T.; Satoh, T. Synthesis of Well-Defined Three- and Four-armed Cage-shaped Polymers *via* "Topological Conversion" from Trefoil- and Quatrefoil- Shaped Polymers. *Macromolecules* **2017**, *50*, 97−106.

(27) Ree, B. J.; Satoh, Y.; Jin, K. S.; Isono, T.; Kim, W. J.; Kakuchi, T.; Satoh, T.; Ree, M. Well-Defined Stable Nanomicelles Self-assembled by Brush Cyclic and Tadpole Copolymer Amphiphiles: A Versatile Smart Carrier Platform. *NPG Asia Materials* **2017**, *9*, e453.

(28) Kim, Y. Y.; Ree, B. J.; Kido, M.; Ko, Y.-G.; Ishige, R.; Hirai, T.; Wi, D.; Kim, J.; Kim, W. J.; Takahara, A.; Ree, M. High Performance n-Type Electrical Memory and Morphology-induced Memory-mode Tuning of A Well-defined Brush Polymer Bearing Perylene Diimide Moieties. *Adv. Electronic Mater.* **2015**, *1*, 1500197.

(29) Ree, B. J.; Aoki, D.; Kim, J.; Satoh, T.; Takata, T.; Ree, M. Macromolecular [2]Rotaxanes Linked with Polystyrene: Properties and Nanoscale Film Morphologies. *Macromolecules* **2019**, *52*, 5325−5336.

(30) Ree, B. J.; Aoki, D.; Kim, J.; Satoh, T.; Takata, T.; Ree, M. Phase Transition Behaviors and Nanoscale Film Morphologies of Poly(δ-valerolactone) Axles Bearing Movable and Fixed Rotaxane Wheels. *Macromol. Rapid Commun*. **2019**, *40*, 1900334

(31) Ree, B. J.; Satoh, Y.; Isono, T.; Satoh, T. Bicyclic Topology Transforms Self-Assembled Nanostructures in Block Copolymer Thin Films. *Nano Lett.* **2020**, *9*, 6520**–**6525.

(32) Marko, J. F. Microphase Separation of Block Copolymer Rings. *Macromolecules* **1993**, *26*, 1442−1444.

(33) Jo, W. H.; Jang, S. S. Monte Carlo Simulation of The Order–disorder Transition of A Symmetric Cyclic Diblock Copolymer System. *J. Chem. Phys.* **1999**, *111*, 1712−1720.

(34) Zhang, G.; Fan, Z.; Yang, Y.; Qiu, F. Phase Behaviors of Cyclic Diblock Copolymers. *J. Chem. Phys.* **2011**, *135*, 174902.

(35) Honda, S.; Koga, M.; Tokita, M.; Yamamoto, T.; Tezuka, Y. Phase Separation and Self-Assembly of Cyclic Amphiphilic Block Copolymers with A Main-chain Liquid Crystalline Segment. *Polym. Chem*. **2015**, *6*, 4167–4176.

(36) Zhu, Y. Q.; Gido, S. P.; Iatrou, H.; Hadjichristidis, N.; Mays, J. W. Microphase Separation of Cyclic Block Copolymers of Styrene and Butadiene and of Their Corresponding Linear Triblock Copolymers. *Macromolecules* **2003**, *36*, 148−152.

(37) Takano, A.; Kadoi, O.; Hirahara, K.; Kawahara, S.; Isono, Y.; Suzuki, J.; Matsushita, Y. Preparation and Morphology of Ring-Shaped Polystyrene-block-polyisoprenes, *Macromolecules* **2003**, *36*, 3045−3050.

(38) Lescanec, R. L.; Hajduk, D. A.; Kim, G. Y.; Gan, Y.; Yin, R.; Gruner, S. M.; Hogen-Esch, T. E.; Thomas, E. L. Comparison of the Lamellar Morphology of Microphase-Separated Cyclic Block Copolymers and Their Linear Precursors. *Macromolecules* **1995**, *28*, 3485−3489.

(39) Poelma, J. E.; Ono, K.; Miyajima, D.; Aida, T.; Satoh, K.; Hawker, C. J. Cyclic Block Copolymers for Controlling Feature Sizes in Block Copolymer Lithography. *ACS Nano* **2012**, *6*, 10845−10854.

(40) The Institute of Electrical and Electronics Engineers, Incorporated., The Roadmap for Devices and Systems, 2020 Edition, https://irds.ieee.org/editions/2020 (accessed June, **2020**).

Graphic Table of Contents

Influence of Topological Confinement on Nanoscale Film Morphologies of Tricyclic Block Copolymers

*Brian J. Ree, Yusuke Satoh, Takuya Isono, and Toshifumi Satoh**